One-dimensional haemodynamic model of a vascular network with fractional-order viscoelasticity

R. Yanbarisov[a b c] and T. Gamilov[a c d e]

Abstract — We propose a computational framework for a one-dimensional haemodynamic model with the arterial walls described by the fractional-order viscoelastic material constitutive law. This framework is used to compare blood flow characteristics for simulations with elastic and fractional-order viscoelastic walls. We use three well-established benchmark tests: a single pulse wave in a long vessel, flow in a 37-segment network of elastic tubes, and flow in anatomically detailed arterial network consisting of 61 arterial segments. All results for elastic model are in a good agreement with analytical solutions, *in vitro* data and other well-established approaches. Fractional-order model demonstrates noticeable differences in pulse wave propagation speed and minor differences in pressure and flow profiles. Differences in profiles are negligible in major vessels, but more profound in vessels beyond the third or fourth generation.

Keywords: Haemodynamics, one-dimensional blood flow, fractional derivative, viscoelasticity, vessel wall

MSC 2010: 92C55, 65D18, 68U10, 37M05, 92B99

Blood flow simulations provide flow patterns and various flow features (pressure, velocity, wall shear stress, etc.) in human vasculature. The values of blood flow and pressure are important for understanding of the progression of vascular diseases. An arterial wall, its properties and behaviour are a major part of blood flow simulations. The arterial wall is a complex heterogeneous structure with various biomechanical properties. Accurate simulation of arterial wall is a challenging task, so the majority of blood flow models utilize numerous simplifications. Solid arterial wall is usually used in three-dimensional simulations [21], which provides satisfactory accuracy for a number of applications. Fluid-structure interactions with various vessel wall models are also used to increase the accuracy when needed [11]. One-dimensional haemodynamic simulations often use constitutional laws, which describe vessel walls by elastic or integer-order viscoelastic models [8, 25]. Elastic

[a]Marchuk Institute of Numerical Mathematics of the Russian Academy of Sciences, Moscow 119333. E-mail: ruslan.yanbarisov@gmail.com

[b]Sechenov University, Moscow 119992

[c]Sirius University of Science and Technology, Sochi 354340

[d]Moscow Institute of Physics and Technology, Dolgoprudny 141701

[e]World–Class Research Center 'Digital biodesign and personalized healthcare', I. M. Sechenov First Moscow State Medical University (Sechenov University), Moscow 119991

vessel walls can be treated as an ideal spring: there is a one-to-one correspondence between blood pressure and vessel cross-sectional area [25, 26]. In models with integer-order viscoelastic walls blood pressure depends on the cross-sectional area and its time derivative [8]. Such viscous properties of a vessel wall material as the energy dissipation is taken into account. Further development involves transition to the fractional-order viscoelastic models, where blood pressure depends on the fractional-order time derivative of the cross-sectional area.

In recent years there has been a growing interest in fractional-order derivatives for blood flow models [6, 12, 23, 29]. Fractional derivatives involve integration over the full trajectory of a particle or a system. As a result, the current state of a system depends on its history represented by its previous states. Such features of fractional-order derivative models as non-locality and memory, which are often described by the single fractional order parameter, enable the complex pressure-flow relations over various time and space scales without the addition of smaller sub-models. For example, introduction of fractional derivatives into the Windkessel model (elastic reservoir model) with the single additional parameter, fractional differentiation order, is sufficient to provide more realistic aortic blood pressure profiles without the need to introduce the representation of systemic circle or additional sub-models of microcirculation [6, 12]. Fractional-order models have also been used to simulate blood flow interactions with a magnetic field [4], viscoelastic vessel walls [10, 23], hypertensive blood pressure profiles [6].

In the present work, we construct a one-dimensional haemodynamic model with the arterial wall described by the fractional-order viscoelastic material. We use mathematical model of one-dimensional blood flow with numerical implementation proposed in [13, 25], and validate resulting computational framework with the help of benchmark tests [8]. Then we modify the presented approach by introducing mathematical formulation of fractional-order vessel wall proposed in [23]. Our goal is to compare flow and pressure profiles for different variants of the model, including the elastic one. Our previous results [12] show that fractional derivatives can be used in boundary conditions to adjust aortic pressure profile and improve personalization of the model. Here, we investigate the impact of fractional derivatives in vessel wall constitutive law for major vessels and for smaller arteries.

1. Haemodynamic model of a vascular network with fractional-order viscoelasticity

1.1. Governing equation for the haemodynamic model with elastic vessels

We consider the following one-dimensional haemodynamic model for blood flow in vessels [13, 25]. This model is based on the flow of the incompressible viscous fluid through a network of one-dimensional tubes. Laws of mass and momentum conservation within the network are expressed as a system of hyperbolic equations for each tube (detailed derivation can be found in [24]):

$$\frac{\partial A}{\partial t} + \frac{\partial Au}{\partial x} = 0 \qquad (1.1)$$

$$\frac{\partial u}{\partial t} + \frac{\partial}{\partial x}\left(\frac{u^2}{2} + \frac{P}{\rho}\right) = -2\pi\mu(2+\xi)\frac{u}{A}. \tag{1.2}$$

Here t is time, x is the coordinate along the vessel, $A = A(x,t)$ is the cross-sectional area, $u = u(x,t)$ is the velocity averaged over the cross section, ξ is the shape profile constant ($\xi = 2$ for the parabolic profile), $P = P(x,t)$ is the blood pressure, ρ and μ are blood density and viscosity, respectively.

In order to solve the system (1.1), (1.2) it is necessary to provide a pressure-area relation. In the case when the wall behaviour is described by the linear isotropic and incompressible elastic material, the pressure-area relation is governed by the Laplace's law and takes the following form [2, 24]:

$$p = \beta\left(\sqrt{A} - \sqrt{A_0}\right) \tag{1.3}$$

where $\beta = \frac{4}{3}\sqrt{\pi}Eh/A_0$. Here E is the Young modulus, h is the wall thickness, r_0 is the lumen radius corresponding to the reference cross-sectional area $A_0 = \pi r_0^2$ at equilibrium state $(A, U, p) = (A_0, 0, p_{\text{ext}})$.

On the inlet vessels such as ascending aorta we specify flux, which is given either by an analytical expression or by tabulated data corresponding to the flux in real patients.

On the outlet of terminal vessels we simulate microcirculation vessels with the three-element Windkessel model by coupling our 1-D model with 0-D Windkessel model:

$$Q\left(1 + \frac{R_1}{R_2}\right) + CR_1\frac{\partial Q}{\partial t} = \frac{P - P_{\text{out}}}{R_2} + C\frac{\partial P}{\partial t}. \tag{1.4}$$

Three-element Windkessel model consists of a resistance R_1 connected in series with a parallel combination of a second resistance R_2 and a compliance C, R_2 is the resistance of the entire systemic vascular bed, which is also called the total peripheral resistance, C is the total arterial compliance, which describes the distensibility of the peripheral arteries and veins. The resistance R_1 is equal to the characteristic impedance of the end point in the arterial network to minimize wave reflections [3].

One-dimensional vessels are connected to each other in junction points to create an arterial structure. The conditions of mass conservation and the total pressure continuity are imposed at the junction points:

$$\sum_k Q_k = 0 \tag{1.5}$$

$$\frac{\rho u_i^2}{2} + P_i = \frac{\rho u_j^2}{2} + P_j, \quad i \neq j. \tag{1.6}$$

Here k denotes indices of all incident vessels, while i and j are the indices of any two incident vessels.
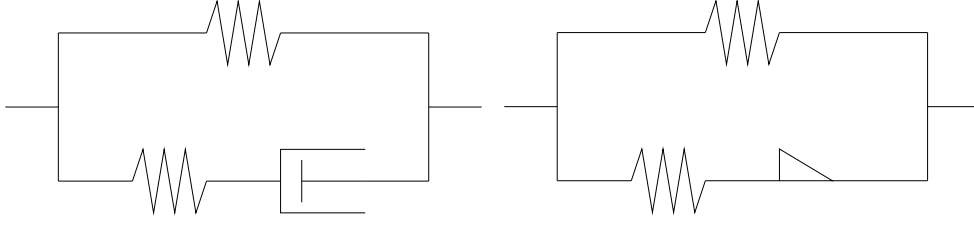
Figure 1. Schematic representation of the SLS model (left) and the FO-SLS model (right). Dashpot component in the SLS model is replaced with the spring-pot in FO-SLS.

1.2. Pressure-area relation for the fractional-order viscoelasticity wall model

We follow [23, 29] to derive the relation between pressure and cross-sectional area of the vessel with viscoelastic walls.

   We assume that the behaviour of the wall material is described by fractional-order standard linear solid (FO-SLS) model. This model is the fractional-order generalization of the standard linear solid (SLS) model, which is constructed using the parallel combination of a spring with a spring in series with a fractional-order dashpot, *spring-pot* (see Fig. 1):

$$\sigma(t) + \frac{\eta}{E_2} D^\alpha \sigma(t) = E_1 \left(\varepsilon(t) + \eta \frac{E_1 E_2}{E_1 + E_2} D^\alpha \varepsilon(t) \right). \tag{1.7}$$

Here

$$D^\alpha u(t) = \frac{1}{\Gamma(1-\alpha)} \int\limits_0^t \frac{\frac{\partial u}{\partial t}(\theta)}{(t-\theta)^\alpha} \, d\theta$$

is the Caputo fractional derivative with $0 < \alpha \leqslant 1$, $\sigma(t)$ is the circumferential tensile stress, $\varepsilon(t)$ is the circumferential strain, E_1, E_2 and η are the elastic moduli and viscosity of the spring-pot for the SLS model, respectively. In the case of $E_2 = 0$ and $\eta = 0$ model reduces to the linear elasticity model with Young modulus equal to E_1.

   Before we can derive pressure-area relation, we need to derive the relation between circumferential tensile stress $\sigma(t)$ and strain $\varepsilon(t)$ from (1.7). We apply the Laplace transform $\mathscr{L}$ to both sides of equation:

$$\left(1 + \frac{\eta}{E_2} s^\alpha\right) \mathscr{L}(\sigma)(s) = E_1 \left(1 + \eta \frac{E_1 E_2}{E_1 + E_2} s^\alpha\right) \mathscr{L}(\varepsilon)(s). \tag{1.8}$$

We introduce relaxation time constant $\tau = \eta/E_2$. Then

$$\mathscr{L}(\sigma)(s) = \left((E_1 + E_2) - \frac{E_2}{\tau} \frac{1}{\tau^{-1} + s^\alpha} \right) \mathscr{L}(\varepsilon)(s). \tag{1.9}$$

Performing inverse Laplace transform gives expression for the stress:

$$\sigma(t) = \left((E_1 + E_2) - \frac{E_2}{\tau} E_{\alpha,\alpha}\left(-\frac{t^\alpha}{\tau}\right) \right) \varepsilon(t). \tag{1.10}$$

Here

$$E_{\alpha,\beta}(z) = \sum_{k=0}^{\infty} \frac{z^k}{\Gamma(\alpha k + \beta)}$$

is the two-parametric Mittag-Leffler function [14] with $\beta = \alpha$.

Circumferential tensile stress $\sigma(t)$ is related to the pressure $p(t)$ inside vessel through the Laplace law [1]:

$$\sigma(t) = \frac{R_0(p(t) - p_0)}{h}. \tag{1.11}$$

Here R_0 and p_0 are arterial radius and pressure at the reference state $(A, p, U) = (A_0, p_0, U_0)$.

The corresponding circumferential strain is [5]:

$$\varepsilon(t) = \frac{4}{3} \frac{R - R_0}{R_0}. \tag{1.12}$$

Substituting (1.11) and (1.12) into (1.10), we obtain the following pressure-area relation for the wall governed by the FO-SLS model [29]:

$$p(t) = \left(1 + \frac{E_2}{E_1}\right) p^E(t) - \frac{1}{\tau} \frac{E_2}{E_1} \int_0^t I(t - \theta) p^E(\theta) \, d\theta \tag{1.13}$$

$$p^E(t) = \frac{4\sqrt{\pi} E_1 h}{3 A_0} \left(\sqrt{A(t)} - \sqrt{A_0} \right) \tag{1.14}$$

$$I(t) = t^\alpha E_{\alpha,\alpha}\left(-\frac{t^\alpha}{\tau}\right). \tag{1.15}$$

The model described above was proposed in [10] and fitted to data obtained from the uniaxial stress-relaxation tests on the tissue of ascending aorta. Eight sets of parameters E_1, E_2, η, and α are presented in Tab. 1. Each set corresponds to a different specimen of aortic tissue of four patients [10]. It was found that large systemic arteries are described by low values of fractional order $\alpha \in [0.1, 0.4]$. This leads to prevalent elastic behaviour of such vessels, which, in turn, provides similar description of flow through these vessels as conventionally used elastic constitutional tube law.

We perform several numerical experiments with different FO-SLS model parameters obtained in [10] and presented in Tab. 1. One of the goals of this work is to compare pressure and flow profiles between linear elastic and FO-SLS wall models.

Table 1. Parameters for the FO-SLS model used in numerical experiments (presented in [10]).

Name	E_1	E_2	η	α
FSLS1	0.68	0.39	2.14	0.23
FSLS2	0.64	0.49	1.80	0.18
FSLS3	0.56	0.48	5.54	0.11
FSLS4	0.61	0.48	1.54	0.16
FSLS5	0.67	0.38	1.88	0.22
FSLS6	0.62	0.51	1.95	0.36
FSLS7	0.80	0.19	3.76	0.10
FSLS8	0.69	0.33	2.77	0.23

In order to compare the results in arteries other than aorta we assume that Young modulus E is given for each vessel for linear elastic wall model. For FO-SLS model of the same artery we assume that $E_1 = E$ and scale E_2 to obtain the same ratio E_2/E_1 as given in Tab. 1. It was assumed for simplicity that each vessel is described by the same parameters of fractional viscoelasticity η, α, E_1, E_2. However, it is well known, that different vessels can possess different elastic and viscoelastic behaviour depending on the location and geometric characteristics such as its diameter and length. There is a lacking amount of data and experiments, which extract FO-SLS parameters for different vessels, which forces us to use parameters obtained for aorta.

1.3. Numerical discretization

We solve the hyperbolic system (1.1), (1.2) inside each vessel numerically with the help of an explicit characteristic method [20], which is monotone and first-order accurate. Compatibility conditions imposed on junctions (1.5), (1.6) and boundary conditions imposed on outlets (1.4) form the system of nonlinear equations, which is solved using the Newton method. Compatibility conditions are discretized implicitly with the first-order approximation in time variable. A detailed description of the numerical discretization can be found in [27].

In order to discretize convolution integral in (1.13), we follow [16]. Consider the convolution integral

$$\int_a^b f(t-\theta)g(\theta)\,\mathrm{d}\theta \tag{1.16}$$

with the restriction that a few values of numerical approximation of function g are available (in our case g provides pressure values at the current and previous time steps), and that inverse Laplace transform of f is known *a priori*.

The algorithm is based on approximating convolution integral effectively via a quadrature rule for contour integration in the complex plane, which appears as the

result of applying inverse Laplace transform to the convolution kernel function [19]:

$$f(t) = \frac{1}{2\pi i} \int_{\Gamma_\ell} F(s) e^{ts} \, ds \approx \sum_{j=-N}^{N} \omega_j^{(\ell)} F(s_j^{(\ell)}) e^{ts_j^{(\ell)}}, \quad t \in I_\ell. \tag{1.17}$$

Here $B > 1$ is the base number, ℓ is the contour index number, Γ_ℓ is the contour in the complex plane chosen to provide an approximation over the time interval $I_\ell = [B^{\ell-1}\Delta t, (2B^\ell - 1)\Delta t]$. In order to approximate the integral in (1.13) for $t \in [0, T]$ with time step Δt it is sufficient to use $L = \lceil \log_B(T/\Delta t + 1)/2 \rceil$ contours, which increases logarithmically with T. Substitution of (1.17) in (1.16) results in:

$$\int_a^b f(t-\theta)g(\theta) \, d\theta = \int_a^b \left(\frac{1}{2\pi i} \int_\Gamma F(s) e^{(t-\theta)s} \, ds \right) g(\theta) \, d\theta$$

$$= \frac{1}{2\pi i} \int_\Gamma F(s) e^{(t-b)\lambda} \left(\int_a^b e^{(b-\theta)s} g(\theta) \, d\theta \right) ds.$$

The inner integral is recognized as the solution $y(b,a,s)$ of the scalar linear initial value problem

$$y' = sy + g, \quad y(a) = 0.$$

If $[t-b, t-a] \subset I_\ell$, then the contour integral over $\Gamma = \Gamma_\ell$ is replaced with the trapezoidal quadrature rule (1.17), which leads to

$$\int_a^b f(t-\theta)g(\theta) \, d\theta \approx \sum_{j=-N}^{N} \omega_j F(z_j) e^{(t-b)s_j} y(b,a,s_j). \tag{1.18}$$

In our case $f(t)$ is given by (1.15) with inverse Laplace transform $F(s) = 1/(s^\alpha + \tau^{-\alpha})$.

We choose $2N+1$ quadrature points independently of ℓ, then fix $B = 5$ and $N = 20$ hereafter, and choose a hyperbola contour

$$z(\theta) = \frac{N}{T_\ell} \mu \left(1 - \sin(i\beta\theta + \alpha)\right)$$

with the choice of parameters, which are optimal for the chosen B and given interval $[t_0, \Lambda t_0]$ (here $t_0 = B^{\ell-1}\Delta t$, $\Lambda = 2B - 1/B^{\ell-1}$), which follows the procedure described in [28]. It is proved that the algorithm computes a convolution integral with the spectral accuracy with respect to the number of points in quadrature rule [18].

During numerical modelling with N time steps it is necessary to evaluate N convolution integrals for each degree of freedom of the vessel. A sequence of fast growing time intervals I_ℓ covering $[\Delta t, T]$ leads to logarithmic amount of contours

used in approximation. This leads to an effective algorithm with $\mathscr{O}(N\log N)$ operations, $\mathscr{O}(\log N)$ Laplace transform evaluations and $\mathscr{O}(\log N)$ memory for each vessel node, which is more efficient than $\mathscr{O}(N^2)$ operations, $\mathscr{O}(N)$ evaluations of Laplace transform and $\mathscr{O}(N)$ memory in the case of direct computations.

The solution procedure at each time step consists of two stages. On the first stage, equation (1.13) is computed using the numerical discretization for the convolution integral described above. On the second stage, a finite difference scheme for equations (1.1), (1.2) is used with the pressure data updated on the first stage to compute the solution on the next time step. Notice that the convolution integral uses pressure data at previous time steps with the weights determined by the kernel function $I(t)$, which decreases, therefore accounting of the memory effects inherent to the models described by the fractional-order derivatives.

2. Numerical experiments

In this work we perform numerical simulations for two distinct setups. The first one is the one-dimensional haemodynamic model with a vessel wall described by the linearized elasticity model (1.3). We refer to it as 'elastic model'. It can be obtained by assuming $E_2 = 0$ in (1.13). The second one is the one-dimensional haemodynamic model with the pressure-area relation for the vessel wall governed by the FO-SLS model (1.13). We refer to it as 'FO-SLS model' for brevity. In this setup we use parameter sets of the FO-SLS model E_1, E_2, η, α presented in Tab. 1.

We perform numerical simulations of the following three benchmark tests:

1. Single pulse propagation in a straight reflection-free vessel [8]. This benchmark test simulates the propagation of a narrow Gaussian-shaped wave in an isolated vessel with uniform parameters. An analytical solution exists in the case of the linearized elasticity model. In this test we compare results of elastic model with the analytical solution.

2. Flow in a network of elastic tubes that includes 37 segments [22]. This network is an experimental 1:1 replica of the 37 largest conduit arteries in the human systemic circulation. Pressure and flow were measured *in vitro* in multiple locations. We compare calculated pressure and flow profiles for elastic model with measured *in vitro* data from [2, 8].

3. Flow in an anatomically detailed arterial network (ADAN56) [7]. This network consists of 56 vessels that represent largest human arteries. We compare calculated pressure and flow profiles for elastic model with profiles obtained with other well-established approaches [8].

In all three benchmarks we first validate our elastic model governed by equation (1.3) (or equation (1.13) with $E_2 = 0$) by comparing obtained results with the reference results from [8]. After that we investigate the behaviour of FO-SLS model governed by equation (1.13) and compare differences in pressure and flow profiles between FO-SLS and elastic models.
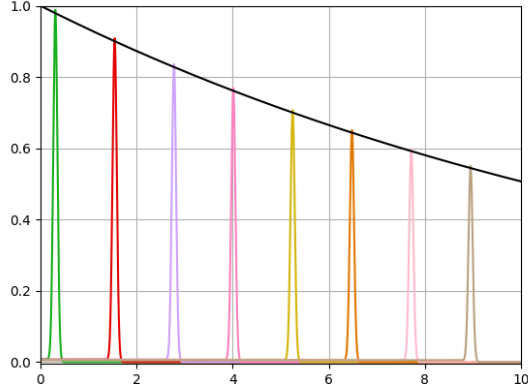
Figure 2. Single pulse wave test. Calculated pressure pulses at different times (coloured lines) and reference analytical solution for the peak pressure height (black line).

Table 2. Parameters for single vessel benchmark.

Parameter	Value
Length, L	10 m
Cross-sectional area, A_0	π cm^2
Initial cross-sectional area, $A(x,0)$	A_0
Initial flow velocity, $U(x,0)$	0
Initial pressure, $P(x,0)$	0
Wall thickness, h	1.5 mm
Blood mass density, ρ	1050 kg m^{-3}
Blood viscosity, μ	4 mPa s
Velocity profile order, ξ	9
Young modulus, E	400 kPa
Diastolic pressure, P_{dia}	0
External pressure, P_{ext}	0
Outflow pressure, P_{out}	0

The model described above was implemented using C++ with OpenMP parallelization.

2.1. Validation of the model with elastic tube law

At first, we consider a single pulse propagation in a vessel with provided analytical input flow, which is given by the Gaussian function

$$Q_{\text{in}}(t) = 10^{-6} \exp\left(-10^4 (t - 0.05)^2\right) \text{ m}^3/\text{s}.$$

At the outflow the pressure is set: $P = P_{\text{out}}$. The vessel is long enough to avoid any reflections from the outflow (right) boundary for the duration of the calculations. The parameters of the benchmark can be found in Tab. 2.

Table 3. Parameters for 37-artery benchmark.

Parameter	Value
Blood mass density, ρ	1050 kg m^{-3}
Blood viscosity, μ	2.5 mPa s
Velocity profile order, ξ	9
Young modulus, E	1.2 MPa
Diastolic pressure, P_{dia}	0
External pressure, P_{ext}	0
Outflow pressure, P_{out}	432.6 Pa

Table 4. Parameters for ADAN56 benchmark.

Parameter	Value
Blood mass density, ρ	1040 kg m^{-3}
Blood viscosity, μ	4.0 mPa s
Velocity profile order, ξ	2
Young modulus, E	225 kPa
Diastolic pressure, P_{dia}	10 kPa
External pressure, P_{ext}	0
Outflow pressure, P_{out}	0

For the presented setup the peak pressure is set from the analytical solution:

$$P_{peak}(x) = P_{peak,0} \exp\left(-\frac{(\xi+2)\pi\mu x}{\rho c_0 A_0}\right). \qquad (2.1)$$

Here $c_0 = 6.17$ m/s is the pulse wave propagation speed in the case of the elastic model and $P_{peak,0}$ is the peak pressure computed for the inviscid case $\mu = 0$.

We set time step $\tau = 10^{-5}$ s and spatial step $h = L/10^4 = 10^{-2}$ cm and consider viscous flow with viscosity $\mu = 4$ mPa s.

Peak pressure profiles obtained during the numerical solution are presented in Fig. 2 along with the analytical profile. It can be observed that numerical peak pressures are in a good agreement with the analytical solution. At any point of time calculated height of the peak (coloured lines in Fig. 2) is very close to the theoretical value (black curve in Fig. 2).

The second benchmark test is a network consisting of 37 silicone vessels presented in [22]. At the inlet of the ascending aorta the periodic flow rate measured *in vitro* is prescribed as the inflow boundary condition $Q_{in}(t)$. Terminal vessels are connected to the outflow pressure through a hydraulic resistance. The 1-D governing equations are solved using the tube law with fully elastic properties with $A_d = A_0$ and $P_d = 0$, and the initial conditions are $(A(x,0), U(x,0), P(x,0)) = (A_0, 0, 0)$ for all segments.

General model parameters for this benchmark are presented in Tab. 3. Details can be found in supplementary materials of [8]. Pressure and flux profiles in several arteries of 37-artery network are presented in Fig. 3. One can see that numerical results are in a good agreement with *in vitro* measurements. There are some differences in smaller vessels (middle and bottom in Fig. 3), but they do not exceed 5% relative error, which is the same deviation reported by authors of other methodologies
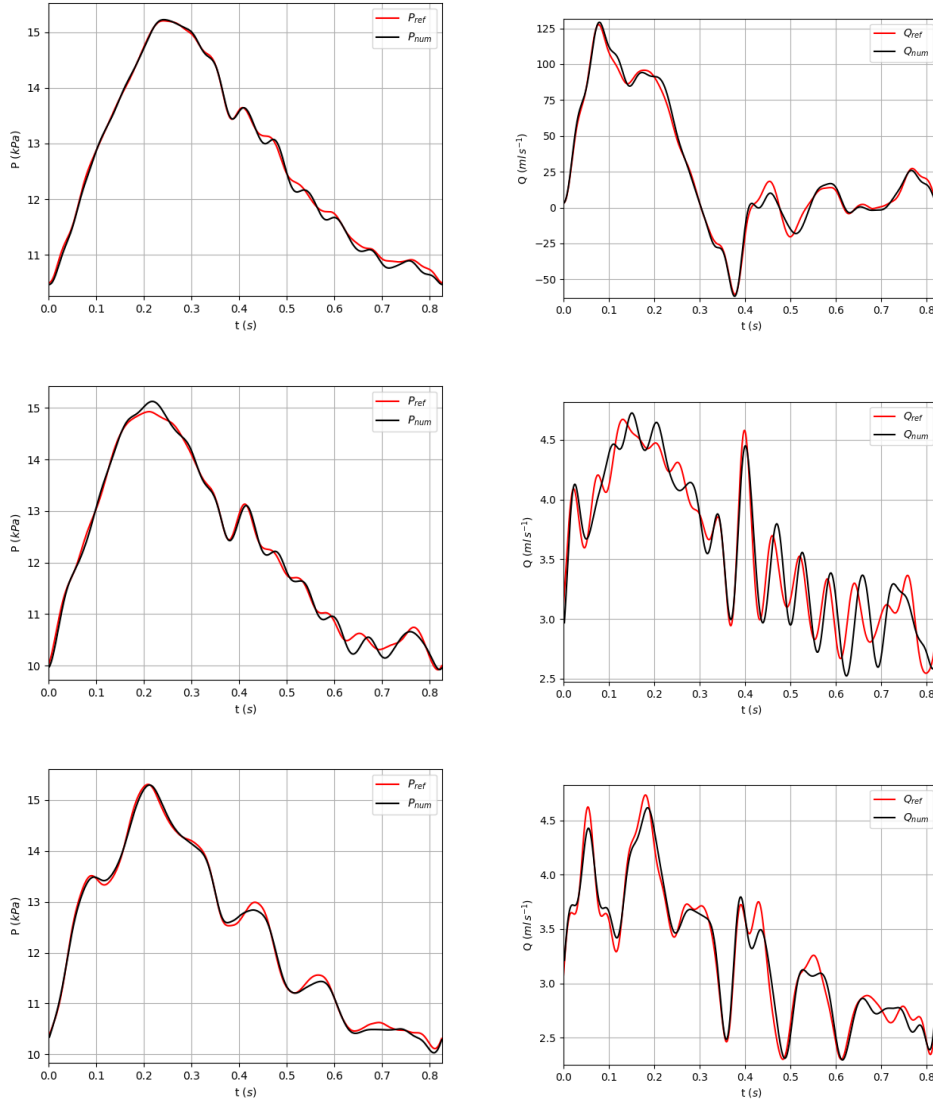
Figure 3. Flow in a 37-artery network. Pressure (left) and flow (right) waveforms in the midpoint of one aortic segments: thoracic aorta II (top), and two vessels from the third generation of bifurcations: right ulnar (middle), splenic (bottom). P_{ref} and Q_{ref} correspond to the *in vitro* data from [8], P_{num} and Q_{num} correspond to numerical data obtained with elastic model in this work.

[8, 22]. We conclude that the computational framework presented in this work does allow us to calculate blood and pressure profiles in the network of elastic tubes.

The third benchmark utilizes a reduced version of the anatomically-detailed arterial network (ADAN56) model developed in [7]. The model contains the largest
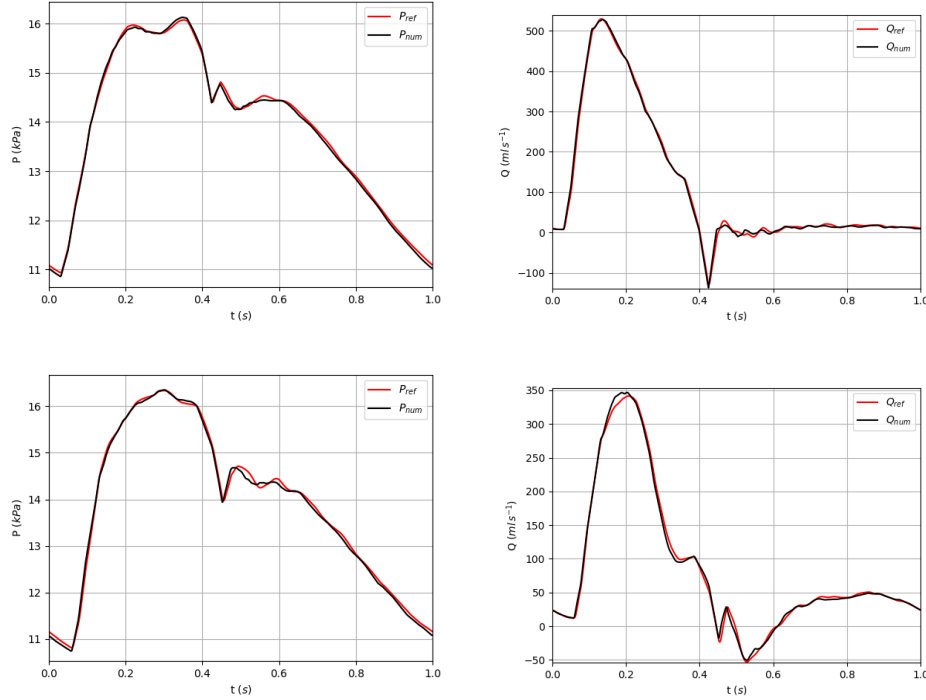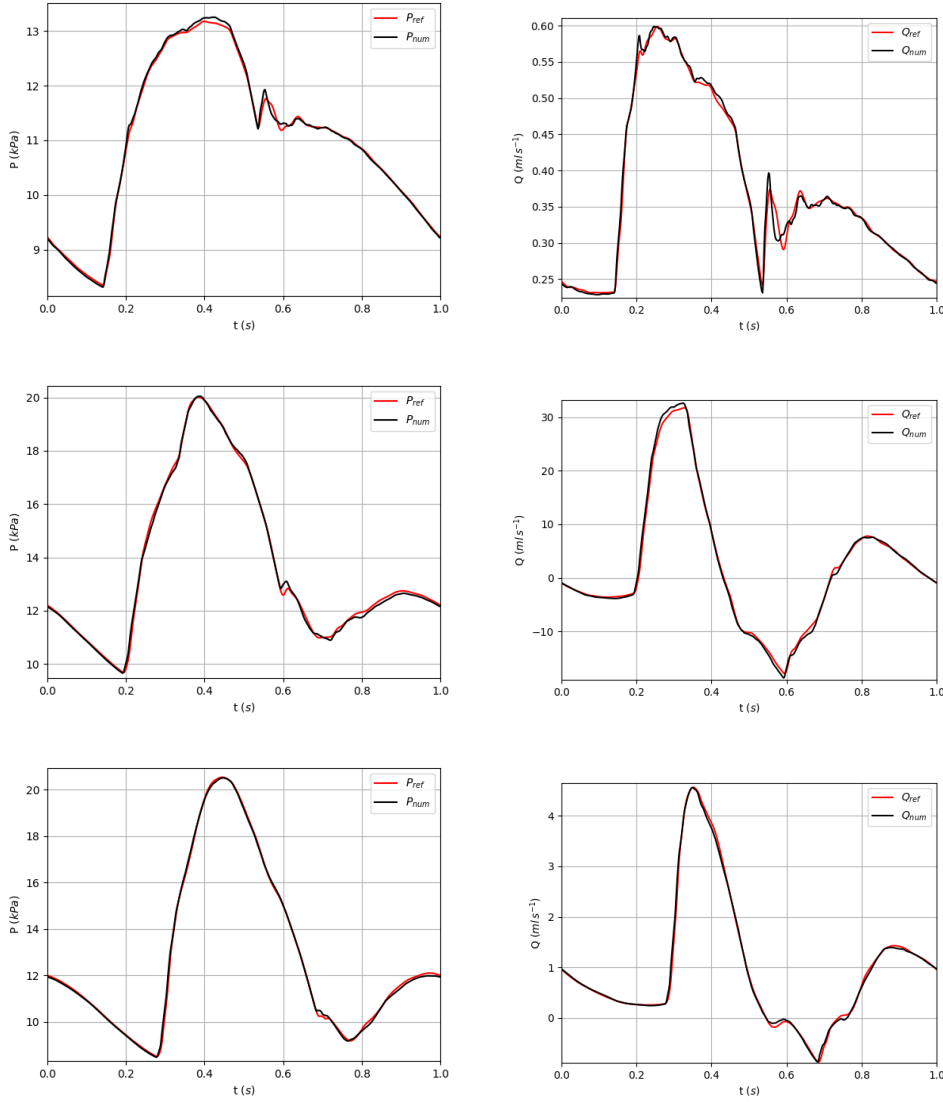
Figure 4. ADAN56 benchmark test. Pressure (left) and flow (right) waveforms in the midpoint of two aortic segments: aortic arch I (top), thoracic aorta III (bottom). P_{ref} and Q_{ref} correspond to the numerical data in [8] (finite-volume method), P_{num} and Q_{num} correspond to the numerical data obtained in this work (grid-characteristic method).

56 vessels of the human arterial system represented by 61 arterial segments. The inflow boundary condition $Q_{\text{in}}(t)$ is given by the periodic inflow function presented in supplementary materials of [8]. Vessel walls are assumed to have the same Young modulus throughout the whole arterial network, $A_d = A_0$, $P_d = P_0 = 10\,\text{kPa}$. Wall thickness is given using empirical relation

$$h = R_0 \left[a \exp(bR_0) + c \exp(dR_0) \right]$$

where R_0 is the reference radius (related to A_0), $a = 0.2802$, $b = -5.053\,\text{cm}^{-1}$, $c = 0.1324$ and $d = -0.1114\,\text{cm}^{-1}$. The initial conditions are $(A(x,0), U(x,0), P(x,0)) = (A_0(x), 0, P_0)$ for all segments. General model parameters for ADAN56 benchmark are presented in Tab. 4.

Pressure and flow profiles in aortic segments (aortic arch and thoracic aorta) of ADAN56 network are presented in Fig. 4. The aortic arch is the closest segment to the inlet of the whole network. The thoracic aorta is approximately 15 cm downstream. We compare our results with profiles obtained using finite-volume method (FVM) from [8]. One can observe that the difference between two approaches is small and does not exceed 1% of systolic pressure (or maximum flow). Figure 5

Figure 5. ADAN56 benchmark test. Pressure (left) and flow (right) waveforms in the midpoint of three vessels from the third and fourth generation of bifurcations: right posterior interosseous (top), right femoral (middle) and right anterior tibial (bottom). P_{ref} and Q_{ref} correspond to the numerical data in [8] (finite-volume method), P_{num} and Q_{num} correspond to the numerical data obtained in this work (grid-characteristic method).

presents profiles for peripheral arteries of ADAN56: right posterior interosseous, right femoral and right anterior tibial. Both approaches provide similar results on peripheral arteries as well.
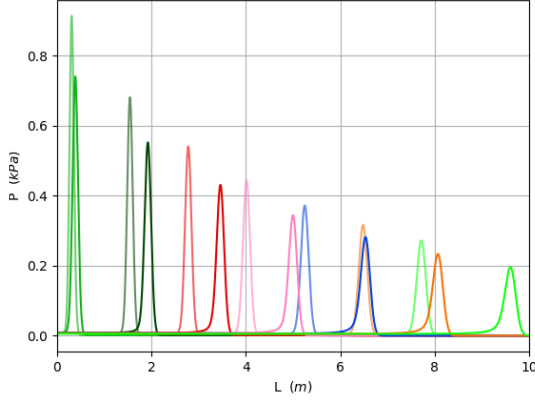
Figure 6. Single pulse wave test. Peak pressure profiles in elastic (blurred lines) and viscoelastic (bright lines) vessel at different times. Same colours correspond to the same time moments.

As we can see from the plots (see Figs. 2–5), the presented computational framework is successfully validated against the analytical solution (first benchmark), *in vitro* measurements (second benchmark) and other well-established computational approaches (third benchmark). In previous validations we only used the elastic model of the vessel wall. In further numerical simulations we use the presented framework to compare the elastic and FO-SLS models.

2.2. Numerical experiments for FO-SLS model of vessel wall

We perform several numerical experiments with different FO-SLS model parameters presented in Tab. 1. In order to compare the results with elastic wall model (1.3) we set $E_1 = E$, where E is a Young modulus of elastic wall, and scale E_2 to obtain the same ratio E_2/E_1 as given in Tab. 1. The remaining parameters ($\tau = \eta/E_2$, α) are set as given in Tab. 1. In all benchmark tests we use the same space and time steps as in the experiments with the elastic model governed by (1.3).

In the first benchmark, we perform a single pulse wave numerical experiment with viscoelastic vessel given by parameters FSLS1 from Tab. 1 and compare resulting pressure profiles for elastic and viscoelastic cases.

It can be seen from Fig. 6 that the pressure profile in the viscoelastic vessel dampens stronger than in elastic case, while moving with the increased speed. For example, when elastic model pulse wave passes 5 m (light-blue) FO-SLS pulse wave is already beyond 6 m mark. The latter means that the pulse wave propagation speed in viscoelastic vessel can be altered in comparison with the elastic case, which might lead to noticeable differences in the network flow simulation results.

It should be noted, however, that in this synthetic benchmark pulse wave moves along the long vessel without any reflections, whereas in real simulations vessels are much shorter, which might alter the behaviour of the pulse wave in the case of short arteries in network simulations.
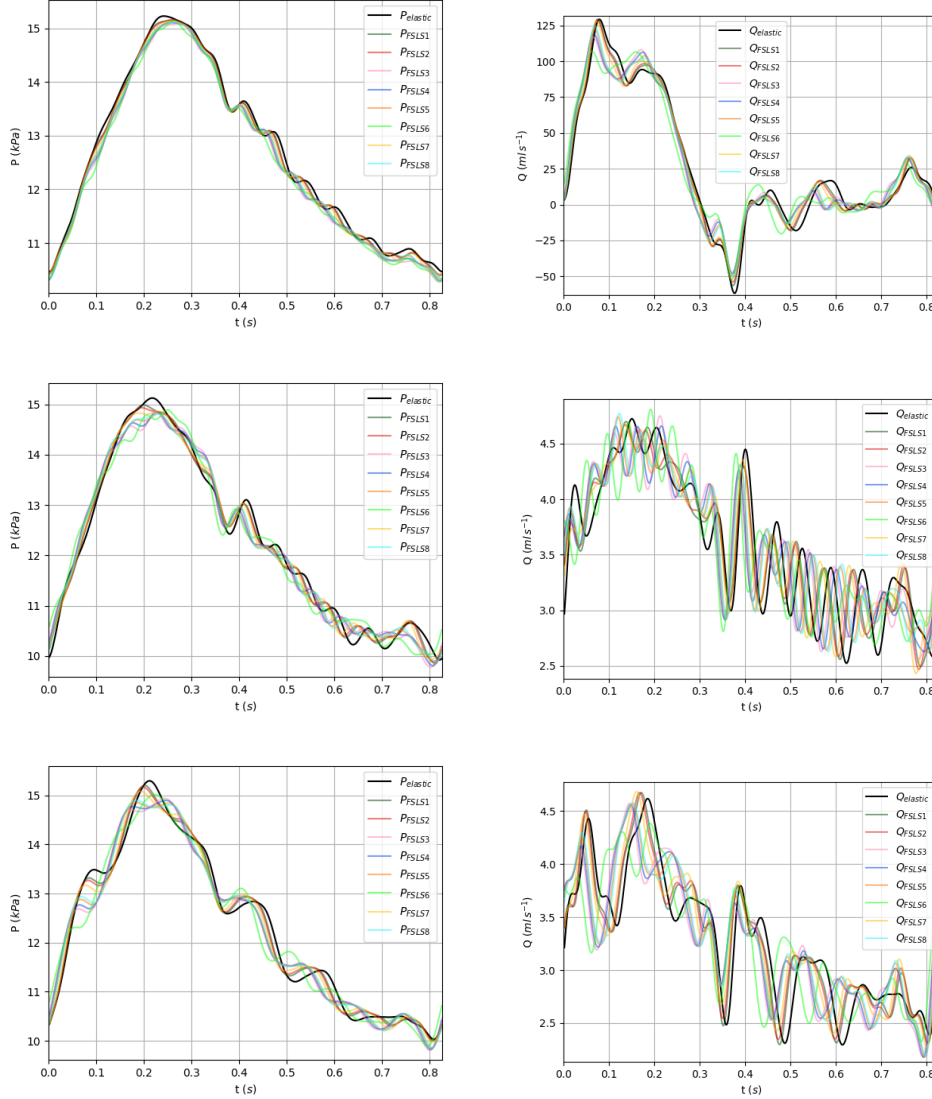
Figure 7. Flow in a 37-artery network. Pressure (left) and flow (right) waveforms in the midpoint of one aortic segments: thoracic aorta II (top), and two vessels from the third generation of bifurcations: right ulnar (middle), splenic (bottom). P_{elastic} and Q_{elastic} correspond to numerical data for simulation with elastic vessel walls, P_{FSLS} and Q_{FSLS} (coloured lines) correspond to numerical data for simulations with viscoelastic vessel walls and parameters presented in Tab. 1.

The second benchmark test involves numerical experiments in a 37-segment network with measured *in vitro* pressure and flow profiles. We perform simulations for eight variants of the FO-SLS model (Tab. 1). Depending on the FO-SLS parameters, a periodic solution can be achieved after different amount of cardiac cycles,
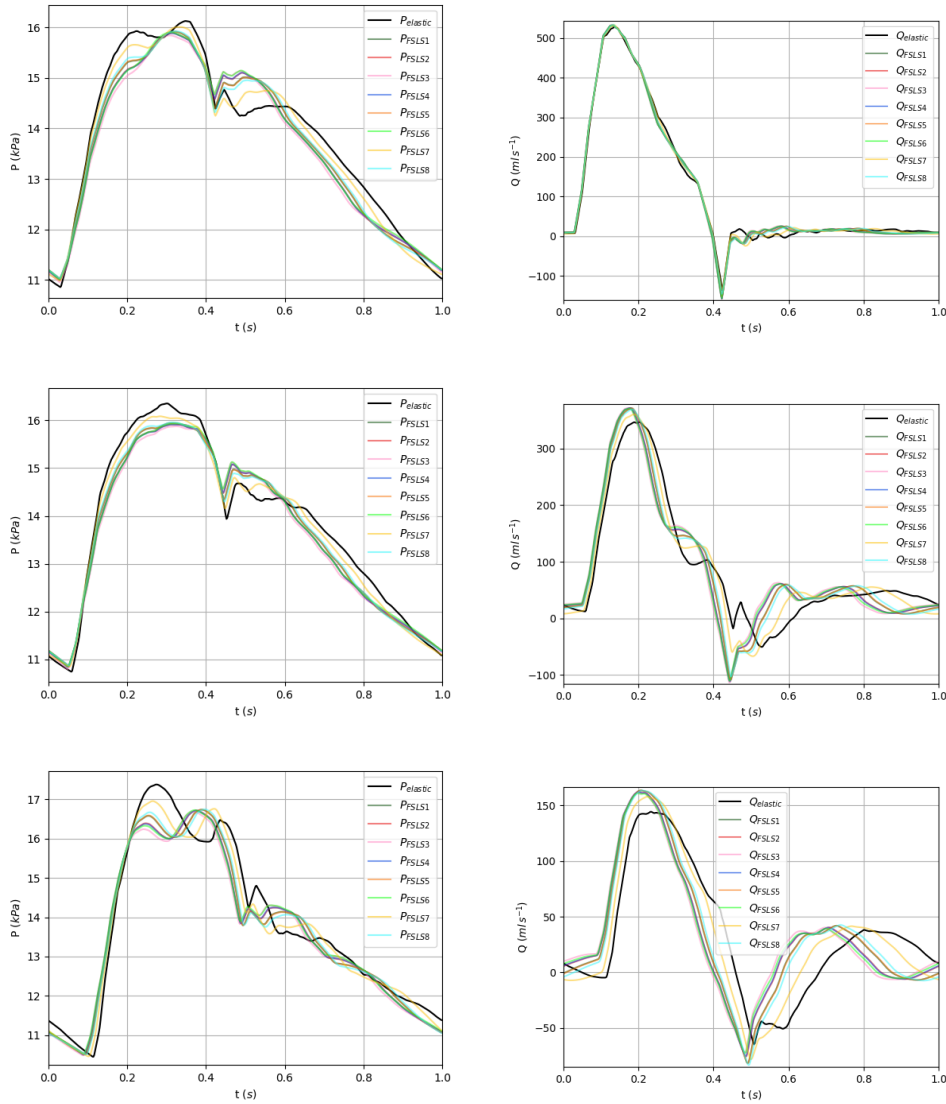
Figure 8. ADAN56 model. Pressure (left) and flow (right) waveforms in the midpoint of three aortic segments: aortic arch I (top), thoracic aorta III (middle) and abdominal aorta V (bottom). P_{elastic} and Q_{elastic} correspond to numerical data for simulation with elastic vessel walls, P_{FSLS} and Q_{FSLS} correspond to numerical data for simulation with viscoelastic vessel walls and parameters presented in Tab. 1.

so we take the one once periodic solution is established. As can be seen from the results presented in Fig. 7, the pressure and flow profiles in arteries located near the aortic input do not significantly differ in shape. There are distinctions between different parameter sets of the FO-SLS model, but maximum and mean pressure

and flow values are similar. The pressure profiles in right ulnar and splenic arteries are also very close. The flow profiles do demonstrate differences: numerous peaks are not synchronized and have various amplitudes. However, average and maximum values throughout the cycle are within 5% margin. The FSLS6 model (light-green line in Fig. 7) appears to demonstrate the most significant deviations from the elastic model (black line in Fig. 7). It may be due to the fact that the FSLS6 model has the highest fractional order $\alpha = 0.36$ (Tab. 1).

Then we perform numerical experiments for the ADAN56 arterial network (third benchmark) with the vessel walls described by the FO-SLS viscoelastic model (1.13). The pressure and flow profiles for three aortic segments are presented in Fig. 8. Figure 9 presents the profiles for peripheral arteries: right posterior inter-osseous, right femoral and right anterior tibial. Similar to the second benchmark, the pressure and flow profiles of the FO-SLS model are very similar to those of the elastic model in the aortic segments. The largest differences are the lowest values of the blood flow (bottom-right and middle-right plots in Fig. 8). The retrograde (backwards) flow increases with the increase of the fractional differentiation order. The ratio between retrograde flow and antegrade flow (RA ratio) is an important diagnostic parameter [17]. Clinical studies show that RA ratio is lower than 10% in the ascending aorta (aortic arch), but increases up to 30% in the thoracic aorta in the healthy case [9, 15, 17]. Our calculations show that for the elastic model RA ratio is 4% in both ascending and thoracic aorta (top-right and middle-right plots in Fig. 8). For FO-SLS model RA ratio is also 4% in ascending aorta, but increases to 10% in thoracic aorta. The absolute value of RA ratio for both elastic and FO-SLS models can easily be adjusted by changing boundary condition at the inlet of the aorta. However, the increase in RA ratio from ascending to thoracic aorta shows that FO-SLS model might be better suited for retrograde flow simulations. Retrograde blood flow during diastole contributes to the coronary and cerebral cir-culations, so FO-SLS model can be important in applications involving coronary or cerebral haemodynamics.

Pressure and flow profiles for peripheral arteries (Fig. 9) demonstrate similar shapes for elastic and FO-SLS models. The following differences can be observed. The first one is the pulse wave propagation speed, which is higher in the case of FO-SLS model. Compared to the aorta, the retrograde flow is not as significant in peripheral arteries. On the contrary, the maximum values of pressure and flow for FO-SLS model can be 10-12% higher than those for the elastic model (black line in Fig. 9). This distinction is important for applications since these are typically the values that can be measured with cuffs or ultrasound. Parameter identification techniques developed for models with elastic vessel walls should be adjusted in case of FO-SLS vessel walls.

The closest FO-SLS model to the elastic model is FSLS7 (orange line in Figs. 8 and 9). This model has the lowest fractional order $\alpha = 0.1$ (Tab. 1). It seems that fractional order is the most important parameter that results in qualitative change in pressure and flow profiles.
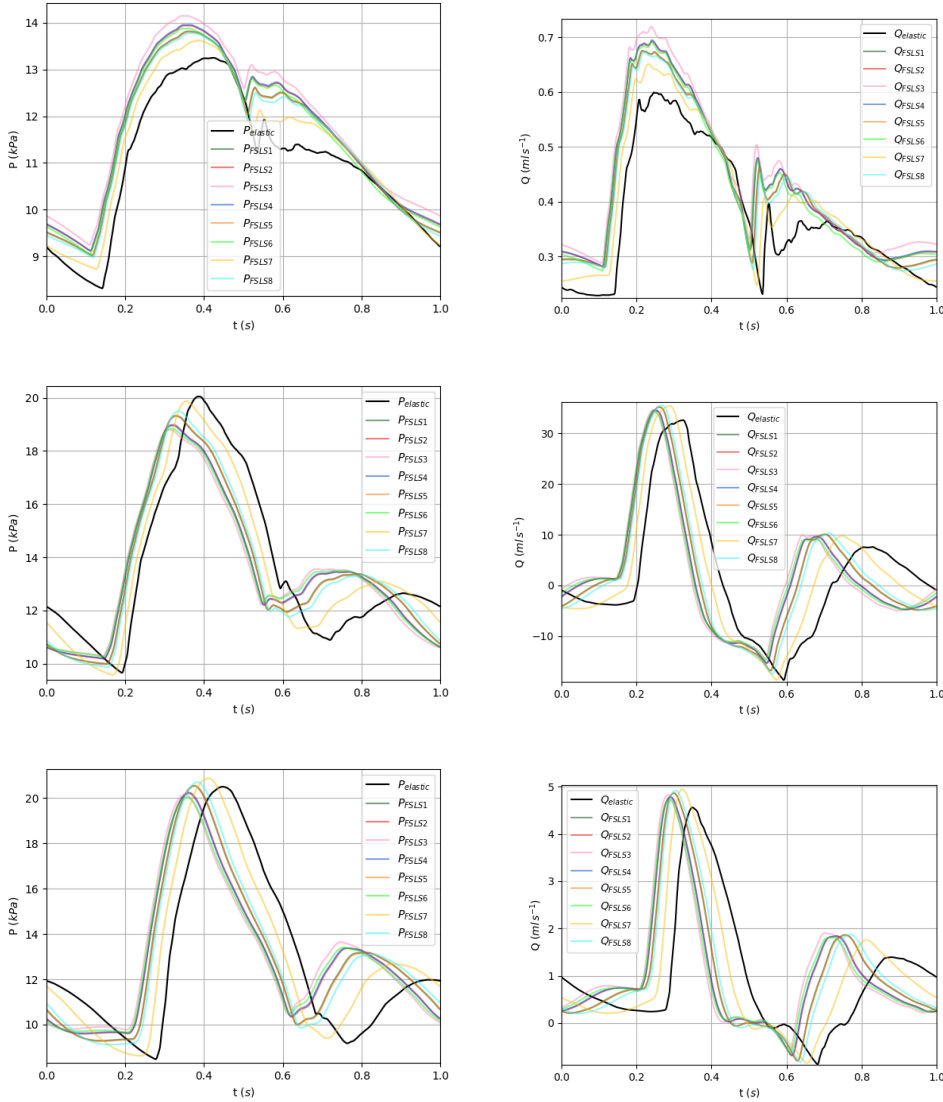
Figure 9. ADAN56 model. Pressure (left) and flow (right) waveforms in the midpoint of three vessels from the third and fourth generation of bifurcations: right posterior interosseous (top), right femoral (middle) and right anterior tibial (bottom). P_{elastic} and Q_{elastic} correspond to numerical data for simulation with elastic vessel walls, P_{FSLS} and Q_{FSLS} correspond to numerical data for simulation with viscoelastic vessel walls and parameters presented in Tab. 1.

In general, numerical flow characteristics in arteries located distantly from the aortic arch can differ significantly in FO-SLS and elastic model simulations. For such arteries FO-SLS model can be considered to be used in simulations, whereas its usage in large arteries located near aortic arch does not justify itself. The only

significant difference in the aortic flow profiles between FO-SLS and elastic model is the retrograde flow, which is more pronounced in FO-SLS model.

3. Conclusions

The prresented one-dimensional model with the elastic and fractional-order viscoelastic tube laws was tested with the help of three well-established benchmark cases. We have demonstrated that pressure and flow profiles in the case of elastic vessel walls correspond to the analytical solution, *in vitro* measurements and results of other well-established approaches.

Numerical simulations for FO-SLS model have demonstrated several distinctions from the elastic model. The first one is the differences in pulse wave propagation speed, which is higher for FO-SLS model. This can be seen from the results of the single pulse propagation test as well as ADAN56 test. The second one is the differences in calculated values of maximum and minimum pressures and flow between elastic and FO-SLS models, which vary depending on the parameters of the latter model and increase with distance from the heart. For arteries up to the fourth generation, these distinctions are not significant, whereas the differences in pressure and flow profiles between elastic and FO-SLS models are substantial in vessels beyond fourth generation. We conclude that it does not worth to use FO-SLS vessel wall model in major arteries, since this model demand substantional computational resources without significant differences in output flow characteristics. However, a fractional-order model could be used to simulate blood flow in the smaller arteries, for example, in the circle of Willis, coronary arteries, and other applications involving arteries with diameters around 1–2 mm.

Most of the quantitative differences between the FO-SLS model and the elastic model can be attributed to proper parameter identification and boundary conditions. Benchmark tests were developed for elastic vessel wall models that work well within small deviations of vessel diameter. Testing non-linear effects of FO-SLS models may require other specialized benchmarks. We observe one qualitative distinction between the FO-SLS model and the elastic model: evolution of retrograde flow along the aorta. Backward flow is more pronounced for the FO-SLS models in thoracic aorta, which corresponds to clinical studies.

It should be noted that fractional-order parameters are difficult to estimate from patient data, which raises the question of the applicability of the model and prospects for its usage. Clinical applications would require a robust parameter identification algorithm for smaller arteries, which leads to expensive invasive tests and experiments with vessel tissue, which are also too complicated to use in everyday practice.

Future work may involve tests in smaller vessels, e.g., calculating pressure drops across stenosis in coronary arteries. Another possible study may involve investigation of vessel adaptation to changes blood flow or pressure. Identification of fractional-order vessel wall parameters is an important task. At this point, it is hard to derive them from patient data. Finally, since computational cost of fractional-

order models is significantly higher due to incorporated non-local and memory effects, the development of effective numerical algorithms is one of the most important task in order to bring this class of models into practical applications.

References

1. J. Alastruey, Numerical modelling of pulse wave propagation in the cardiovascular system: development, validation and clinical applications. *PhD Thesis*. Univ. of London, 2006.

2. J. Alastruey, A. W. Khir, K. S. Matthys, P. Segers, S. J. Sherwin, P. R. Verdonck, K. H. Parker, and J. Peir, Pulse wave propagation in a model human arterial network: assessment of 1-D viscoelastic simulations against in vitro measurements. *Journal of Biomechanics* **44** (2011), No. 12, 2250–2258.

3. J. Alastruey, S. Moore, K. Parker, T. David, J. Peiró, and S. Sherwin, Reduced modelling of blood flow in the cerebral circulation: coupling 1-D, 0-D and cerebral auto-regulation models. *Int. J. Numer. Meth. Fluids* **56** (2008), No. 8, 1061–1067.

4. N. Ali Shah, D. Vieru, and C. Fetecau, Effects of the fractional order and magnetic field on the blood flow in cylindrical domains. *Journal of Magnetism and Magnetic Materials* **409** (2016), 10–19.

5. H. Atabek, Wave propagation through a viscous fluid contained in a tethered, initially stressed, orthotropic elastic tube. *Biophysical Journal* **8** (1968), No. 5, 626–649.

6. M. A. Bahloul, Y. Aboelkassem, and T.-M. Laleg-Kirati, Human hypertension blood flow model using fractional calculus. *Frontiers in Physiology* **13** (2022).

7. P. J. Blanco, S. M. Watanabe, M. A. R. Passos, P. A. Lemos, and R. A. Feijóo, An anatomically detailed arterial network model for one-dimensional computational hemodynamics. *IEEE Trans. Biomed. Eng.* **62** (2014), No. 2, 736–753.

8. E. Boileau, P. Nithiarasu, P. J. Blanco, L. O. Müller, F. E. Fossan, L. R. Hellevik, W. P. Donders, W. Huberts, M. Willemet, and J. Alastruey, A benchmark study of numerical schemes for one-dimensional arterial blood flow modelling. *Int. J. Numer. Meth. Biomed. Eng.* **31** (2015), No. 10, e02732.

9. H. G. Borgen et al, Quantitation of antegrade and retrograde blood flow in the human aorta by magnetic resonance velocity mapping. *American Heart Journal* **117** (1989), No. 6, 1214–1222.

10. D. Craiem, F. Rojo, J. Atienza, G. Guinea, and R. L. Armentano, Fractional calculus applied to model arterial viscoelasticity. *Latin American Applied Research* **38** (2008), No. 2, 141–145.

11. D. Craiem, F. Rojo, J. Atienza, G. Guinea, and R. L. Armentano, On the impact of fluid structure interaction in blood flow simulations. *Vietnam J. Math.* **49** (2021), 169–187.

12. T. Gamilov and R. Yanbarisov, Fractional-order windkessel boundary conditions in a one-dimensional blood flow model for fractional flow reserve (FFR) estimation. *Fractal and Fractional* **7** (2023), No. 5, 373.

13. T. Gamilov, F. Liang, P. Kopylov, N. Kuznetsova, A. Rogov, and S. Simakov, Computational analysis of hemodynamic indices based on personalized identification of aortic pulse wave velocity by a neural network. *Mathematics* **11** (2023), No. 5, 1358.

14. R. Gorenflo, A. A. Kilbas, F. Mainardi, S. V. Rogosin, *et al.*, *Mittag-Leffler Functions, Related Topics and Applications*. Springer, 2020.

15. T. Hasegawa, Y. Oshima, T. Tanaka, A. Maruo, and H. Matsuhisa, Clinical assessment of diastolic retrograde flow in the descending aorta for high-flow systemic-to-pulmonary artery shunting. *The Journal of Thoracic and Cardiovascular Surgery* **151** (2016), No. 6, 1540–1546.

16. R. Hiptmair and A. Schädle, Non-reflecting boundary conditions for Maxwells equations. *Computing* **71** (2003), 265–292.

17. H.-L. Kim, Y. N. Kim, H.-J. Kim, W.-H. Lim, J.-B. Seo, S.-H. Kim, M.-A. Kim, and J.-H. Zo, The value of diastolic flow reversal in the descending thoracic aorta as a determinant of invasively measured aortic pulse pressure. *Echocardiography* **34** (2017), No. 5, 649–655.

18. M. López-Fernández, C. Lubich, and A. Schädle, Adaptive, fast, and oblivious convolution in evolution equations with memory. *SIAM J. Sci. Comput.* **30** (2008), No. 2, 1015–1037.

19. C. Lubich and A. Schädle, Fast convolution for nonreflecting boundary conditions. *SIAM J. Sci. Comput.* **24** (2002), No. 1, 161–182.

20. K. Magomedov and A. Kholodov, *Grid-Characteristic Numerical Methods*. Nauka, Moscow, 1988 (in Russian).

21. M. Mamatyukov, I. Mikheev, D. Parshin, A. Khe, A. Cherevko, K. Orlov, and A. Chupakhin, Comprehensive research of human brain hemodynamics: Clinical monitoring and computer simulations. *AIP Conference Proceedings* **2027** (2018), No. 11, 020009.

22. K. S. Matthys, J. Alastruey, J. Peiró, A. W. Khir, P. Segers, P. R. Verdonck, K. H. Parker, and S. J. Sherwin, Pulse wave propagation in a model human arterial network: assessment of 1-d numerical simulations against in vitro measurements. *Journal of Biomechanics* **40** (2007), No. 15, 3476–3486.

23. P. Perdikaris and G. E. Karniadakis, Fractional-order viscoelasticity in one-dimensional blood flow models. *Annals of Biomedical Engineering* **42** (2014), 1012–1023.

24. S. Sherwin, V. Franke, J. Peiró, and K. Parker, One-dimensional modelling of a vascular network in space-time variables. *J. Eng. Math.* **47** (2003), 217–250.

25. S. Simakov, T. Gamilov, F. Liang, and P. Kopylov, Computational analysis of haemodynamic indices in synthetic atherosclerotic coronary networks. *Mathematics* **9** (2021), No. 18, 2221.

26. Y. Vassilevski, V. Salamatova, and S. Simakov, On the elasticity of blood vessels in one-dimensional problems of hemodynamics. *Comput. Math. and Math. Phys.* (2015), No. 55, 1567–1578.

27. Y. Vassilevski, M. Olshanskii, S. Simakov, A. Kolobov, and A. Danilov, *Personalized Computational Hemodynamics: Models, Methods, and Applications for Vascular Surgery and Antitumor Therapy*. Academic Press, 2020.

28. J. Weideman and L. Trefethen, Parabolic and hyperbolic contours for computing the bromwich integral. *Mathematics of Computation* **76** (2007), No. 259, 1341–1356.

29. Y. Yu, P. Perdikaris, and G. E. Karniadakis, Fractional modeling of viscoelasticity in 3D cerebral arteries and aneurysms. *J. Comput. Phys.* **323** (2016), 219–242.